

Supporting Information

Fabrication of Layered Double Hydroxide Microcapsules Mediated by Cerium Doping Metal-Organic Framework for Boosting Water Splitting

Huajie Xu^{a,b}, Changfu Shan^a, Xiaoxia Wu^a, Mingzi Sun^c, Bolong Huang^{*,c}, Yu Tang^{*,a}, and Chun-Hua Yan^{*,a}

^a State Key Laboratory of Applied Organic Chemistry, Key Laboratory of Nonferrous Metal Chemistry and Resources Utilization of Gansu Province, College of Chemistry and Chemical Engineering, Lanzhou University, Lanzhou, China.

E-mail: yan@lzu.edu.cn; tangyu@lzu.edu.cn

^b School of Chemical and Material Engineering, Fuyang Normal University, Fuyang, China.

^c Department of Applied Biology and Chemical Technology, The Hong Kong Polytechnic University, Hung Hum, Kowloon, Hong Kong SAR, China.

E-mail: bhuan@polyu.edu.hk

Table of Contents

1. Experimental Section

- 1.1 Synthesis of MIL-88A particles.
- 1.2 Synthesis of hollow Ni-Fe-LDH hollow microcapsules
- 1.3 Synthesis of hollow Ni-Fe-Ce-LDH hollow microcapsules.
- 1.4 Synthesis of hollow Ni-Fe-Tb (La, Pr, Eu, Tb, Dy and Lu) LDH
- 1.5 Synthesis of Ce-Ni-LDH

2. Material Characterizations

3. Electrochemical Measurements

4. Calculation Setup

5. Supplementary Figures

Fig. S1. XRD patterns of MIL-88A and Ni-Fe-Ce-LDH

Fig. S2. N₂ adsorption-desorption isotherm of the Ni-Fe-Ce-LDH

Fig. S3. EDX spectrum of Ni-Fe-Ce-LDH

Fig. S4. a, SEM and b, TEM images of the 50%Ce-Ni-Fe-LDH hollow microcapsule

Fig. S5. O 1s XPS spectra of 5%Ce-Ni-Fe-LDH and 50%Ce-Ni-Fe-LDH

Fig. S6. SEM images of Ce-doped MIL-88A obtained by adding different volumes of Ce ions into the synthetic solution for MIL-88A. a, Fe/Ce = 1:0, b, Fe/Ce = 0.9:0.1, c, Fe/Ce = 0.7:0.3, d, Fe/Ce = 0.5:0.5

Fig. S7. XRD patterns of MIL-88A and Ce-doped MIL-88A

Fig. S8. SEM images of Ni-Fe-Ce-LDH obtained by adding different volumes of urea into the synthetic solution. a, 0.0 mM, b, 1.2 mM, c, 2.4 mM, d, 3.6 mM, e, 4.8 mM, f. 6.0 mM.

Fig. S9. TEM images of the Ni-Fe-Ce-LDH obtained by adding 6 mM of urea into the synthetic solution.

Fig. S10. XPS spectra of Ce 3d for 30%Ce-Ni-Fe-LDH

Fig. S11. SEM images of a, Ni-Fe-La-LDH, b, Ni-Fe-Pr-LDH, c, Ni-Fe-Eu-LDH, d, Ni-Fe-Tb-LDH, e, Ni-Fe-Dy-LDH and f, Ni-Fe-Lu-LDH

Fig. S12. EDX spectra of La, Pr, Eu, Dy and Lu doped complexes prepared by the same method

Fig. S13. a, SEM and b, TEM images of the Ni-Fe-Tb-LDH hollow microcapsule

Fig. S14. XRD patterns of 30% Tb-Ni-Fe-LDH

Fig. S15. EDX spectrum of Ni-Fe-Tb-LDH

Fig. S16. HAADF-STEM image and Elemental mapping images of Ni-Fe-Tb-LDH hollow microcapsules.

Fig. S17. Typical cyclic voltammetry curves of **a**, Ni-Fe-LDH, **b**, 10%Ce-Ni-Fe-LDH, **c**, 20%Ce-Ni-Fe-LDH, **d**, 30%Ce-Ni-Fe-LDH in 1M KOH with different scan rates.

Fig. S18. Nyquist plots obtained by EIS at 1.55 V (vs. RHE) of Ni-Fe-LDH and 30%Ce-Ni-Fe-LDH (inset: equivalent RC circuit model).

Fig. S19. XRD spectra of 30%Ce-Ni-Fe-LDH before and after the OER reaction.

Fig. S20. The SEM of 30%Ce-Ni-Fe-LDH after 24 h test.

Fig. S21. a, The top view and side view of pristine MIL-88A. b, The PDOS of pristine MIL-88A

6. Supplementary Tables

Table S1. The relative atom contents of elements in Ni-Fe-Ce-LDH/CNT from ICP-AES data

Table S2. Comparison of catalytic performance with reported MOF-Derived catalyst

Table S3. Comparison of catalytic performance with reported LDH catalyst

Table S4. The TOF of the as-prepared catalysts.

7. References

1. Experimental Section

1.1 Synthesis of MIL-88A particles

All the chemicals were directly used after purchase without further purification. Typically, 69.6 mg of fumaric acid and 262.6 mg of $\text{Fe}(\text{NO}_3)_3 \cdot 6\text{H}_2\text{O}$ were dissolved in 15 mL of deionized water at room temperature to form a clear yellow solution, the mixed solution was transferred into a 20 mL Teflon-lined stainless autoclave and control temperature rise and drop through the program maintaining at 110°C for 6 h. The precipitates were separated by centrifuging, washed with distilled water and ethanol three times in turn, and then dried at 60°C for 1 day.

1.2 Synthesis of hollow Ni-Fe-LDH hollow microcapsules

The obtained MIL-88A was dispersed in 4 mL of ethanol (solution A). 150 mg of $\text{Ni}(\text{NO}_3)_2 \cdot 6\text{H}_2\text{O}$ and 100 mg of urea were dissolved in 6 mL of deionized water (solution B). Then, solution A and solution B were mixed via stirring at room temperature (solution C). At last, the solution C was sealed in a glass bottle, and heated at 90 °C for 6 h without stirring. The product was washed with deionized water and ethanol 3 times by centrifugation and dried at 60°C for 1 day.

1.3 Synthesis of hollow Ni-Fe-Ce-LDH hollow microcapsules

Typically, 69.6 mg of fumaric acid and 288 mg of urea were dissolved in 15 mL of deionized water via stirring at room temperature. $\text{Ni}(\text{NO}_3)_2 \cdot 6\text{H}_2\text{O}$ (567 mg), $\text{Ce}(\text{NO}_3)_3 \cdot 6\text{H}_2\text{O}$ and $\text{Fe}(\text{NO}_3)_3 \cdot 9\text{H}_2\text{O}$ were added in turn, and the total amount of $\text{Ce}(\text{NO}_3)_3 \cdot 6\text{H}_2\text{O}$ and $\text{Fe}(\text{NO}_3)_3 \cdot 9\text{H}_2\text{O}$ is fixed at 0.65 mM in the synthesis of different ratios of Ni-Fe-Ce-LDH. The mixed solution was transferred into a 20 mL Teflon-lined stainless autoclave and control temperature rise and drop through the program maintaining at 110°C for 6 h. The precipitates were separated by centrifuging, washed with distilled water and ethanol three times in turn, and then dried at 60°C for 1 day.

1.4 Synthesis of hollow Ni-Fe-Tb (La, Pr, Eu, Tb, Dy and Lu) LDH

The synthesis procedure is the same as that of Ni-Fe-Ce-LDH hollow microcapsules, only replacing Ce with Tb, La, Pr, Eu, Tb, Dy and Lu.

1.5 Synthesis of Ce-Ni-LDH

The synthesis procedure is the same as that of Ni-Fe-Ce-LDH hollow microcapsules with replacing Fe with Ce completely. The XRD analysis showed that Ce-Ni-LDH did not form the main structure of LDHs

2. Material Characterizations

Transmission electron microscopy (TEM), high-resolution transmission electron microscopy (HRTEM) and elemental mapping were performed on a JEOL JEM 2100 TEM (200kV). Scanning electron microscopy was performed on Carl Zeiss. The chemical compositions were investigated by energy dispersive X-ray spectroscopy (EDX). X-ray diffraction (XRD) patterns were collected on an X'Pert ProX-ray diffractometer with Cu K α radiation ($\lambda = 0.1542$ nm) (40 kV and 40 mA). X-ray photoelectron spectroscopy (XPS) spectra were recorded on a VG ESCALAB 220I-XL device and corrected using C1s line at 284.6 eV. The Brunauer–Emmett–Teller (BET) specific surface area was determined using N₂ adsorption-desorption on an Autosorb-IQ2-MPC system, and the pore size distribution was computed based on quenched solid density functional theory using the adsorption branch.

3. Electrochemical Measurements

Electrochemical measurements were carried out in a typical three-electrode glass cell connected to a CHI 760E Electrochemical Workstation (CHI Instruments, Shanghai Chenhua Instrument Corp., China), comprising a platinum foil counter electrode, a saturated Hg/HgO reference electrode, and a glassy carbon working electrode coated with electrocatalysts. The catalysts were uniformly cast onto a glassy carbon electrode. Before each test, the working electrode was fabricated as follows. 5.0 mg electrocatalysts were first dispersed in 0.95 mL

ethanol, and then 0.05 mL Nafion solution (5.0 wt%) was added, followed by 1.0 h sonication. 10.0 μL suspension was pipetted onto a glassy carbon electrode, which was mechanically polished and ultrasonically washed in advance. Ultimately, the working electrode was prepared after solvent evaporation in the air for 10.0 min. All potentials were calculated with respect to reversible hydrogen electrode (RHE) based on: $E(\text{RHE}) = E(\text{Hg/HgO}) + 0.059 \times \text{pH} + 0.098 \text{ V}$. The overpotential (η) was calculated by $\eta(\text{V}) = E(\text{RHE}) - 1.23\text{V}$. Linear sweep voltammetry (LSV) and cyclic voltammetry (CV) measurements were recorded at a scan rate of 1 mV s^{-1} . The potential was calibrated with respect to a reversible hydrogen electrode (RHE) in 1 M KOH solution. 1M KOH solution was bubbled for about fifteen minutes to saturate it before each test. The ECSA was measured by cyclic voltammetry (CV) using the same working electrodes at a potential window of 0.3-0.4 V vs. RHE in 1 M aqueous KOH solution. CV curves were obtained at different scan rates of 20, 40, 60, 80, 100, 120, 140, 160 and 180 mV s^{-1} . After plotting charging current density differences ($\Delta J = J_a - J_c$ at the potential of 0.3 V) versus the scan rates, the slope, twice of the double-layer capacitance C_{dl} , is used to represent the ECSA. To test the stability of catalysts, a galvanostatic measurement at a fixed current density (J) of 10 mA cm^{-2} was performed. AC impedance spectroscopy was acquired in a frequency range from 100 kHz to 0.1 Hz at an amplitude of 10 mV. The TOF was calculated by the equation: $\text{TOF} = (J \times S) / (4 \times F \times m)$, where J represents the current density (A cm^{-2}) at an overpotential of 300 mV, S and m represent the area of the electrode and the number of moles of the active materials. S (cm^2) is the surface area of glassy carbon electrode, F is the Faraday constant ($96,485 \text{ C mol}^{-1}$), and m is the number of moles of the cations assuming all of them are catalytically active.

4. Calculation Setup

All the calculations are performed by the density functional theory (DFT) within the CASTEP codes^{S1}. The ultrasoft pseudopotential scheme has been chosen with the generalized

gradient approximation (GGA) and Perdew-Burke-Ernzerhof (PBE) for the exchange-correlation energy, in which the 410 eV cut-off energy is applied^{S2-S5}. For all the geometry optimizations, the Hellmann-Feynman forces will be converged to less than 0.001 eV/Å while the total energy has been converged to 5×10^{-5} eV per atom. The Gamma k-point has been applied for the energy minimization based on the Broyden-Fletcher-Goldfarb-Shannon (BFGS) algorithm^{S6-S7}. For all the elements, we have selected the (4*f*, 5*d*, 6*s*), (3*d*, 4*s*, 4*p*), (3*d*, 4*s*, 4*p*), (2*s*, 2*p*), (2*s*, 2*p*), and (1*s*) states as the valence states for Ce, Ni, Fe, C, O, and H atoms, respectively. To guarantee sufficient space for the adsorption of intermediates, we have set 20 Å vacuum space in the z-axis.

For the initial modeling of MIL-88A, the model has been constructed based on the experimental characterization, which includes 134 atoms in total (C₆₆O₆₆Fe₆). The six Fe atoms locate in the octahedral center of 6[FeO₆] while the rest C and O atoms construct the frame of MIL-88A. For the Ce insertion, we have considered three possible conditions of Ce doping, including two different substitution concentration of Fe sites and the vacancy pore site near [FeO₆]. The energy cost of the doping and the related electronic structures have been considered for comparison. The NiFeLDH model has been cleaved from the (003) surfaces of the NiFeLDH unit cell. For the Ce-doped NiFeLDH, the Ce doping atoms evenly replace both Ni and Fe atoms with a concentration of 26%, which is close to the Ce concentration in the experiments of 30%. For the adsorption of different reactants and intermediates, different active sites are considered on the Ce-doped NiFeLDH surfaces. The energetic trend of the OER has considered the adsorption of the reactants, intermediates, and final products based on the optimal adsorption strength.

5. Supplementary Figures

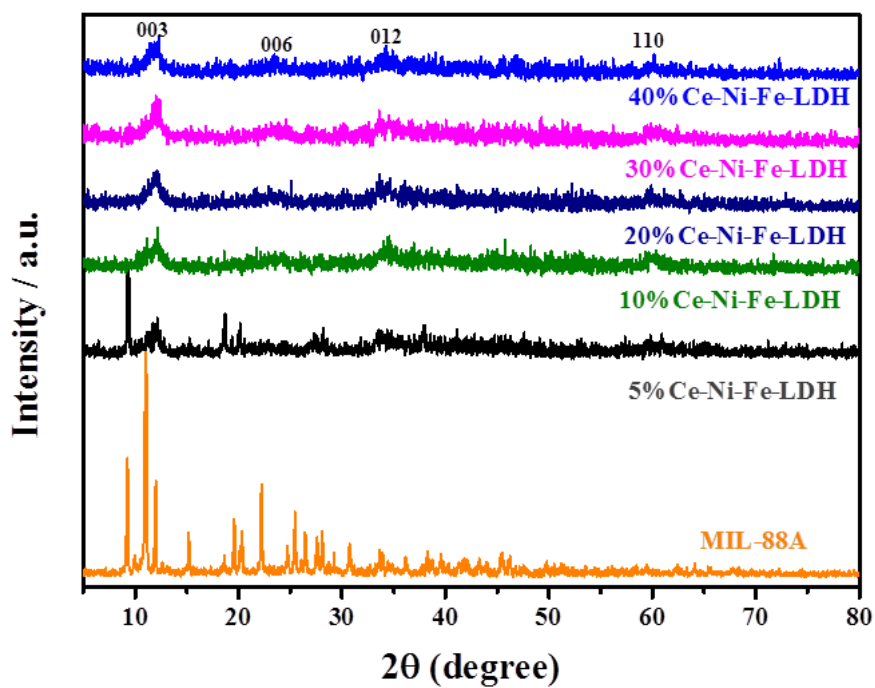


Fig. S1 XRD patterns of MIL-88A and Ni-Fe-Ce-LDH.

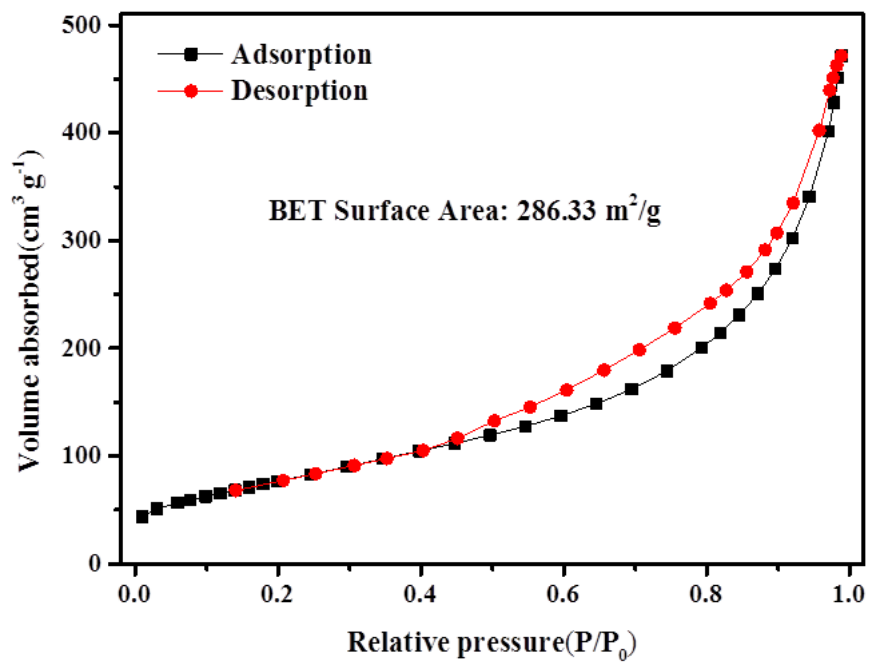


Fig. S2 N_2 adsorption-desorption isotherm of the Ni-Fe-Ce-LDH.

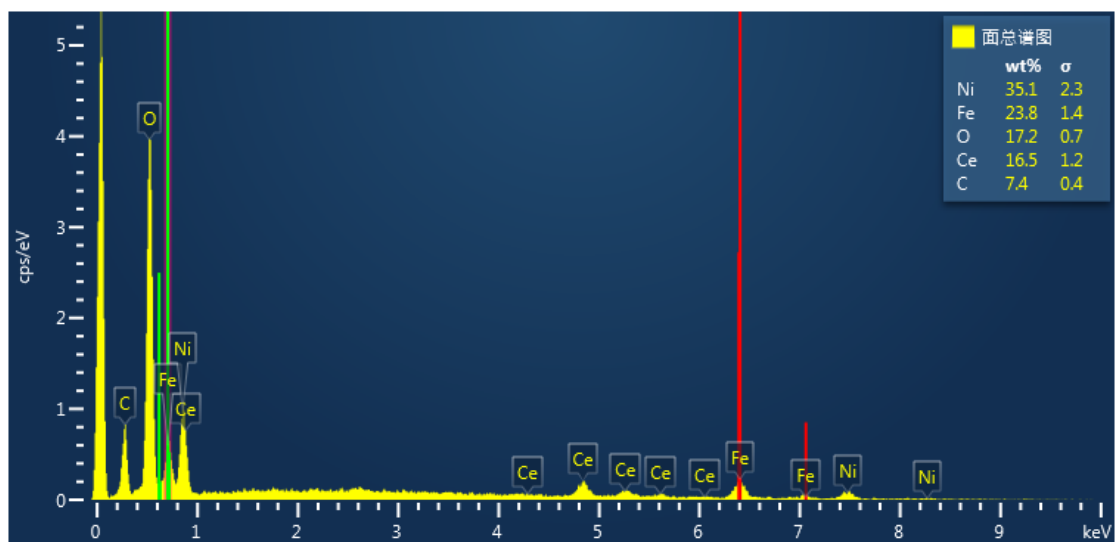


Fig. S3 EDX spectrum of Ni-Fe-Ce-LDH.

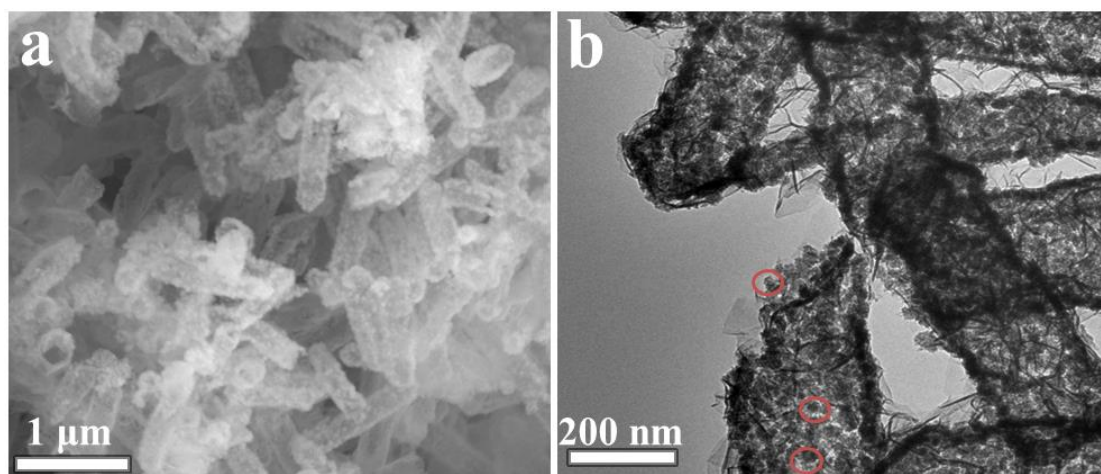


Fig. S4 a, SEM and b, TEM images of the 50%Ce-Ni-Fe-LDH hollow microcapsules.

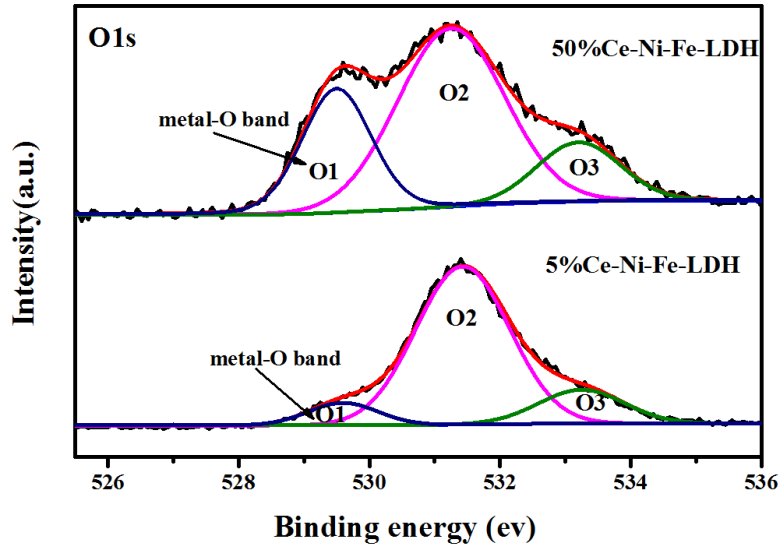


Fig. S5 O 1s XPS spectra of 5%Ce-Ni-Fe-LDH and 50%Ce-Ni-Fe-LDH.

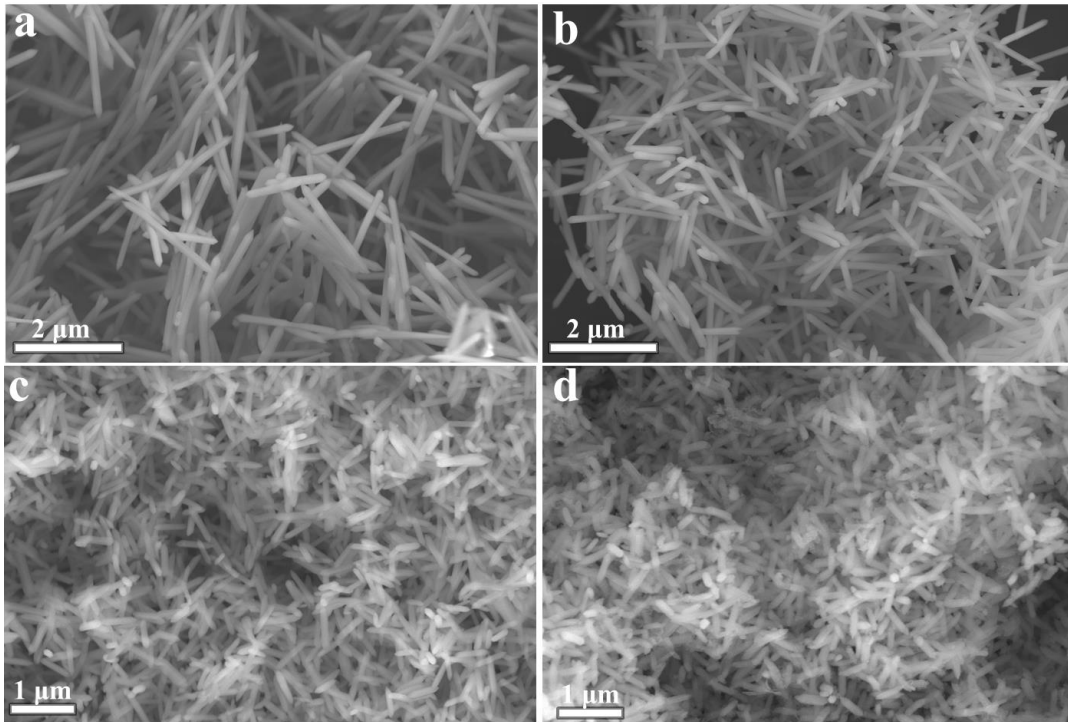


Fig. S6 SEM images of Ce-doped MIL-88A obtained by adding different volumes of Ce ions into the synthetic solution for MIL-88A. a, Fe/Ce = 1:0, b, Fe/Ce = 0.9:0.1, c, Fe/Ce = 0.7:0.3, d, Fe/Ce = 0.5:0.5.

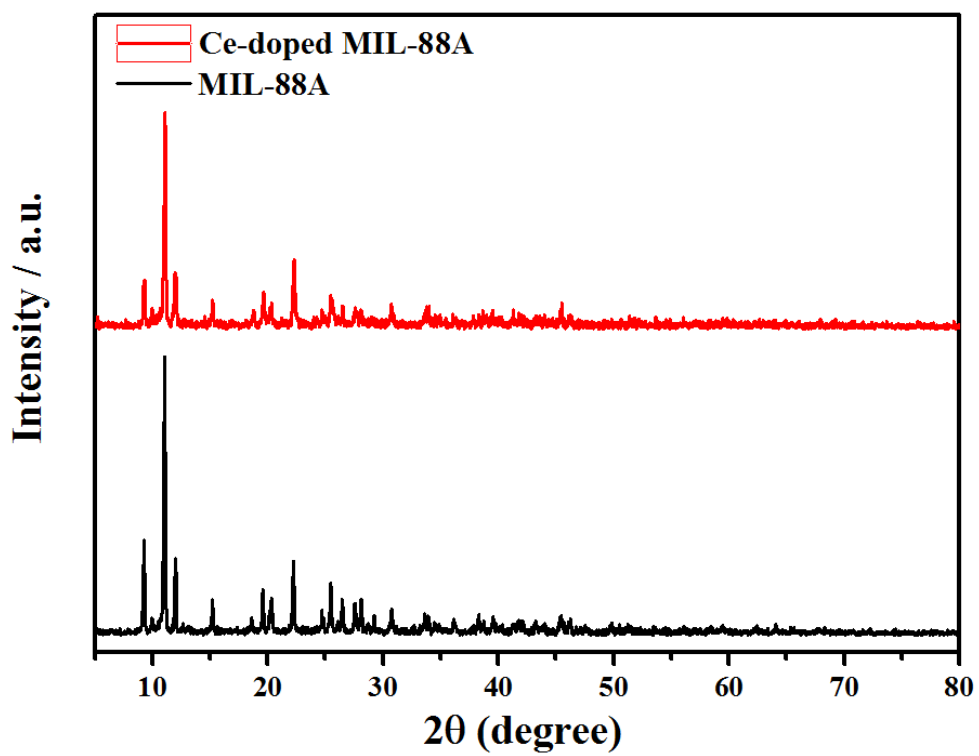


Fig. S7 XRD patterns of MIL-88A and Ce-doped MIL-88A.

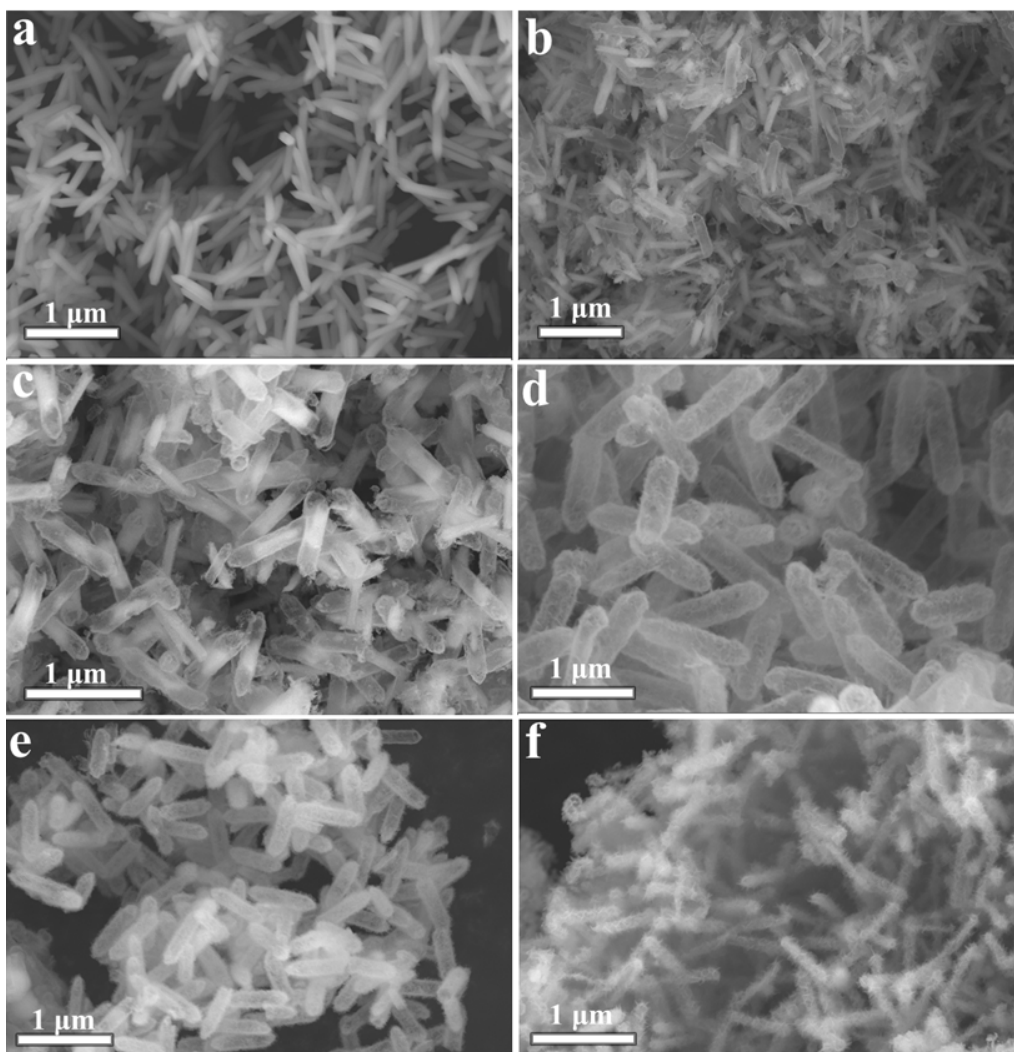


Fig. S8 SEM images of Ni-Fe-Ce-LDH obtained by adding different volumes of urea into the synthetic solution. a, 0.0 mM, b, 1.2 mM, c, 2.4 mM, d, 3.6 mM, e, 4.8 mM, f. 6.0 mM.

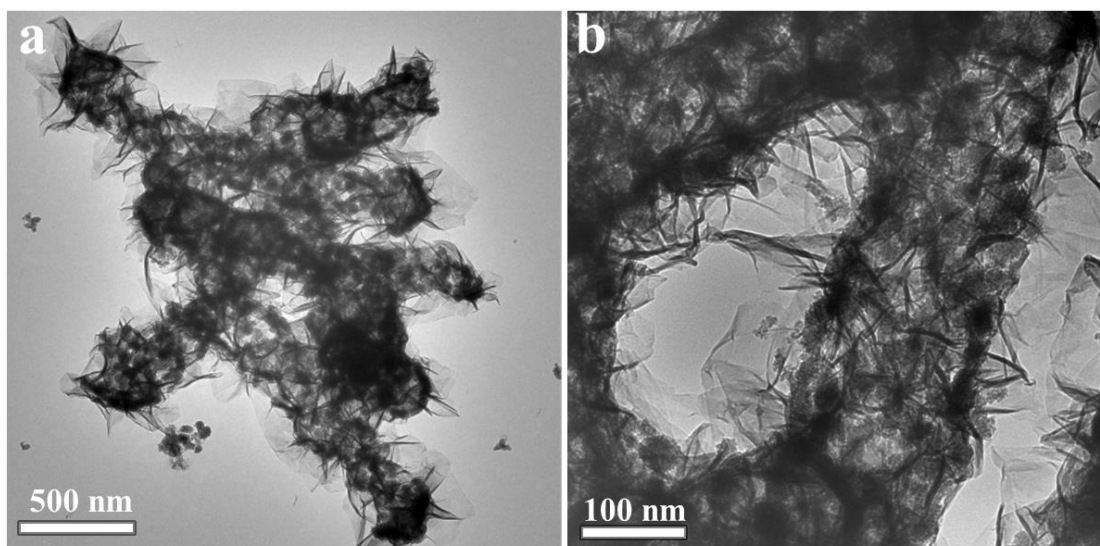


Fig. S9 TEM images of the Ni-Fe-Ce-LDH obtained by adding 6 mM of urea into the synthetic solution.

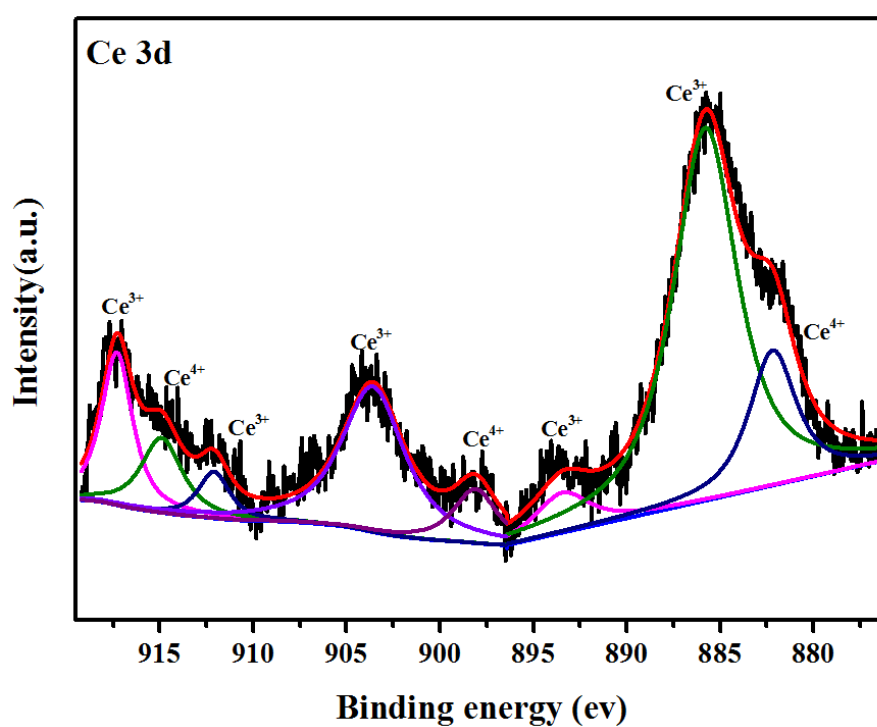


Fig. S10 XPS spectrum of Ce 3d for 30%Ce-Ni-Fe-LDH.

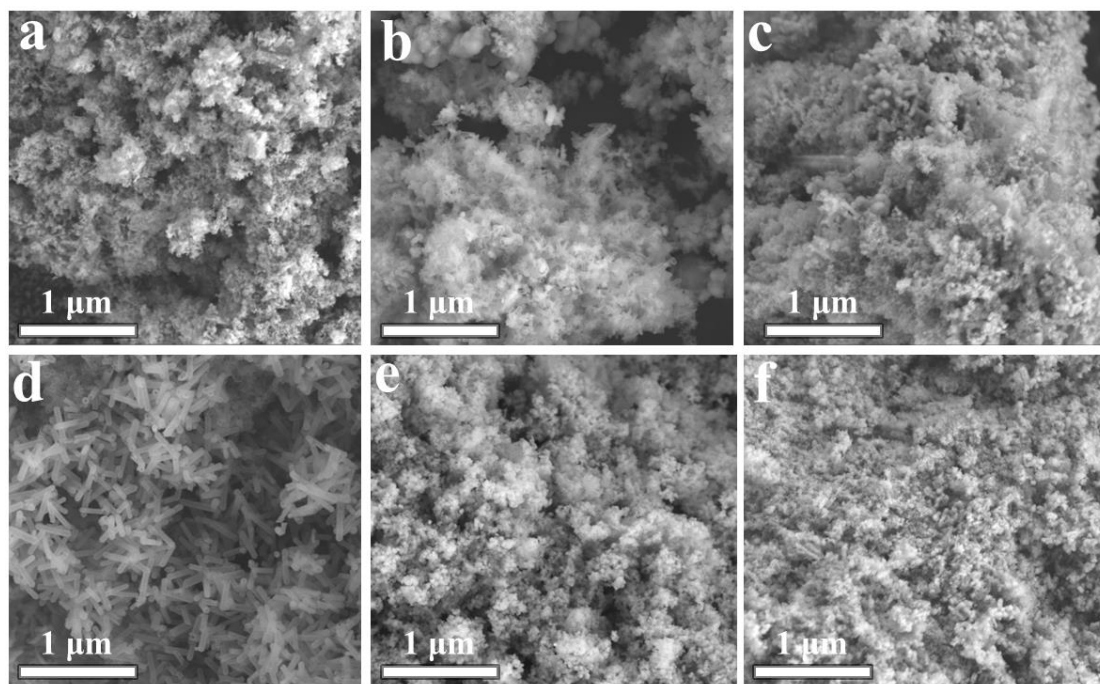


Fig. S11 SEM images of a, Ni-Fe-La-LDH, b, Ni-Fe-Pr-LDH, c, Ni-Fe-Eu-LDH, d, Ni-Fe-Tb-LDH, e, Ni-Fe-Dy-LDH and f, Ni-Fe-Lu-LDH.

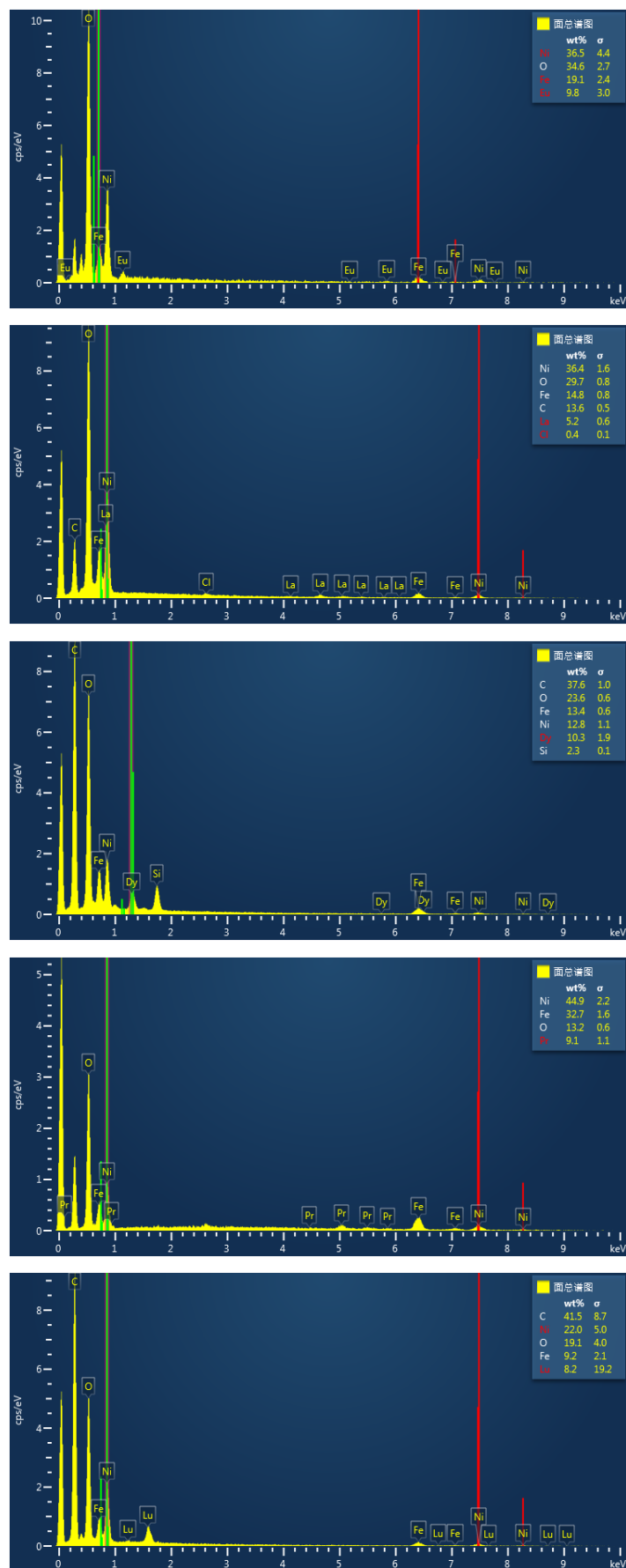


Fig. S12 EDX spectra of La, Pr, Eu, Dy and Lu doped complexes prepared by the same method.

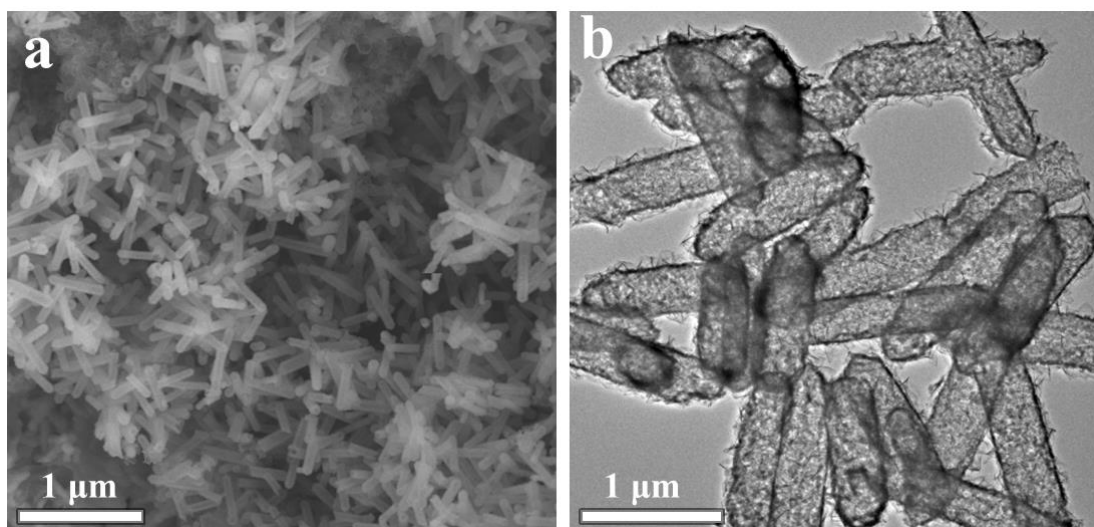


Fig. S13 a, SEM and b, TEM images of the Ni-Fe-Tb-LDH hollow microcapsules.

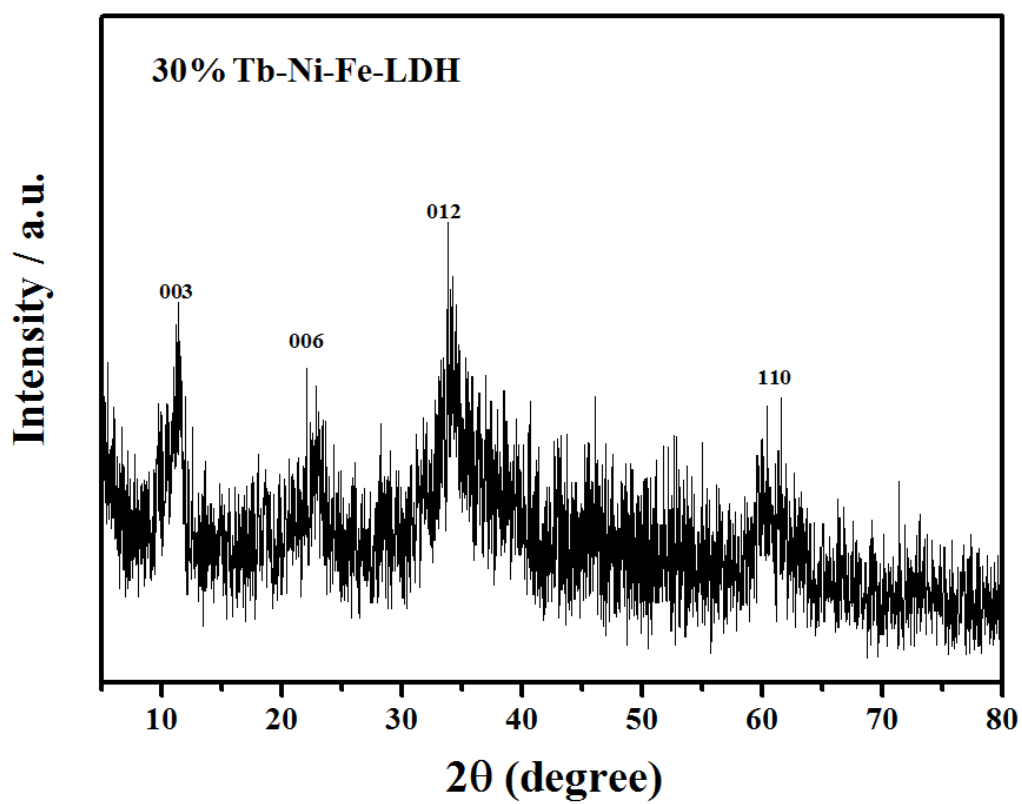


Fig. S14 XRD pattern of 30% Tb-Ni-Fe-LDH.

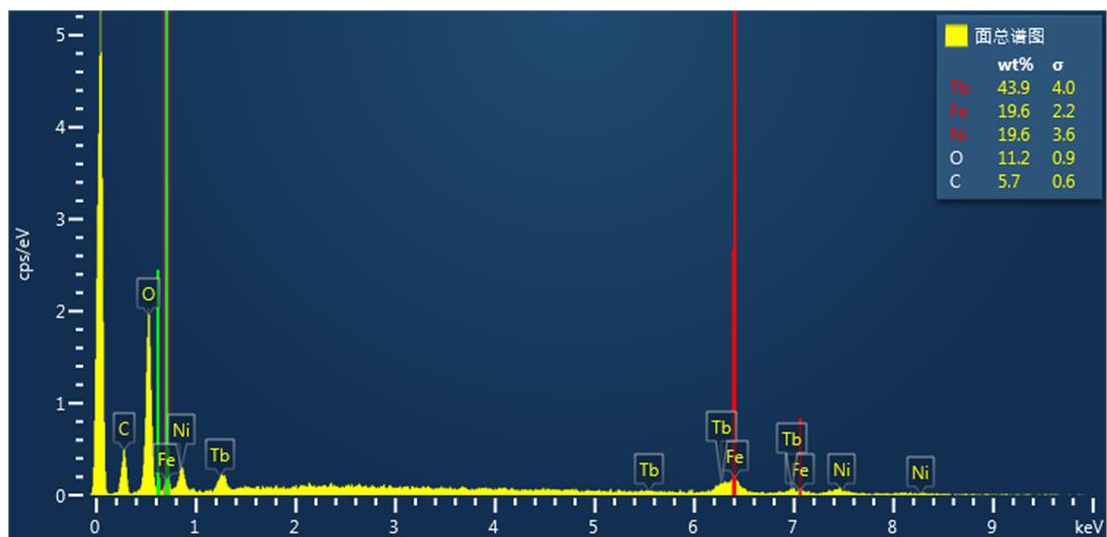


Fig. S15 EDX spectrum of Ni-Fe-Tb-LDH.

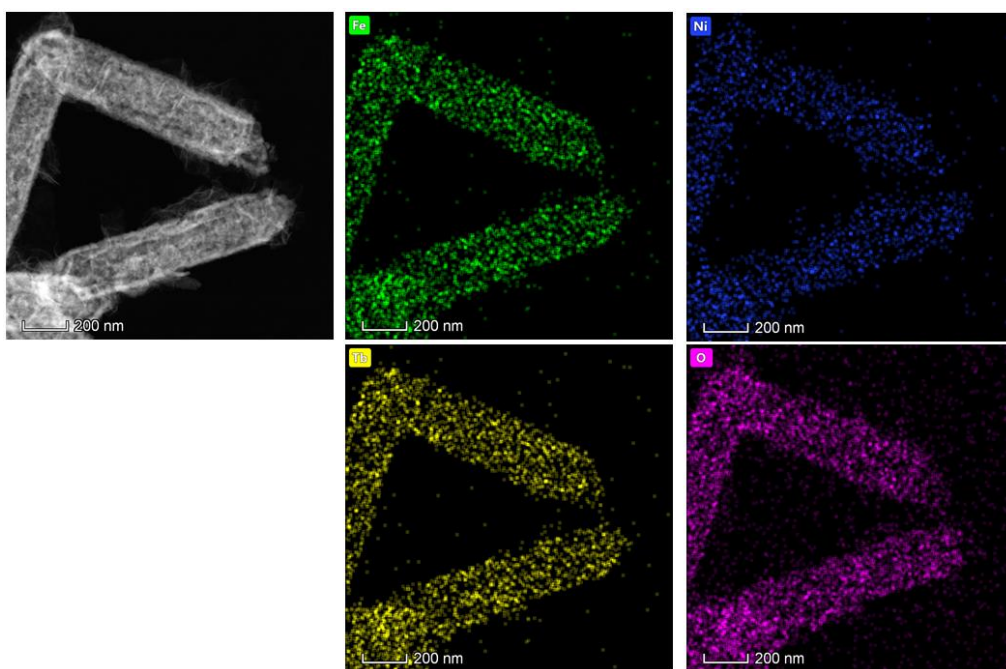


Fig. S16 HAADF-STEM image and elemental mapping images of Ni-Fe-Tb-LDH hollow microcapsules.

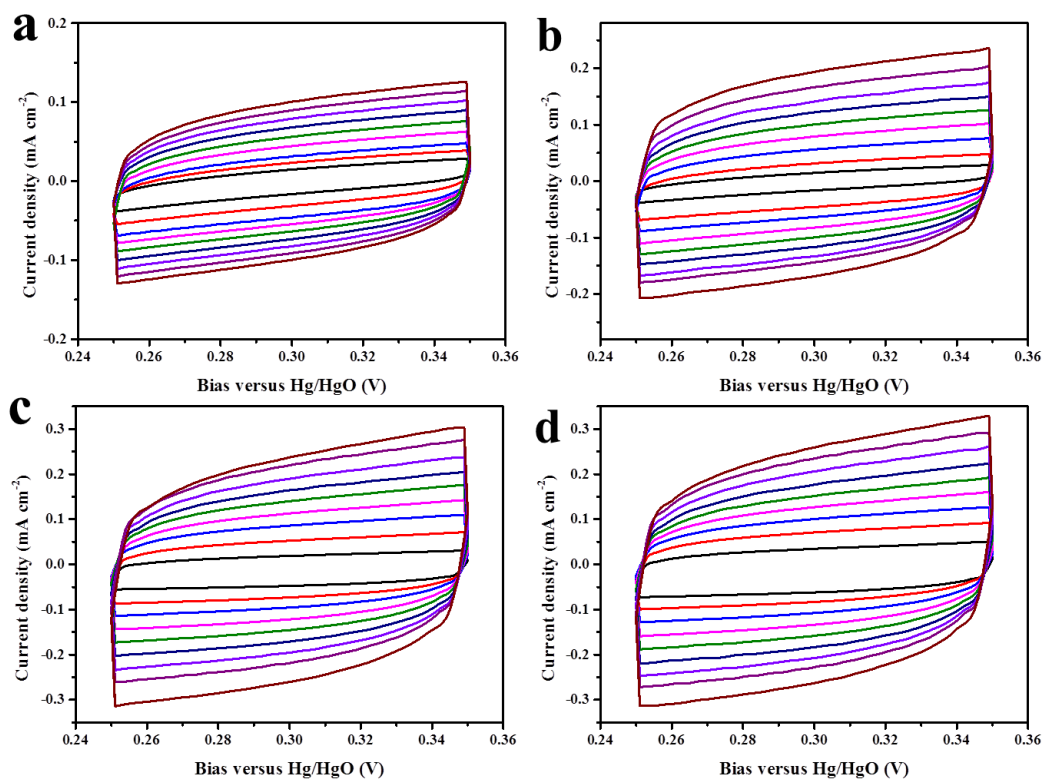


Fig. S17 Typical cyclic voltammetry curves of a, Ni-Fe-LDH, b, 10%Ce-Ni-Fe-LDH, c, 20%Ce-Ni-Fe-LDH, d, 30%Ce-Ni-Fe-LDH in 1M KOH with different scan rates.

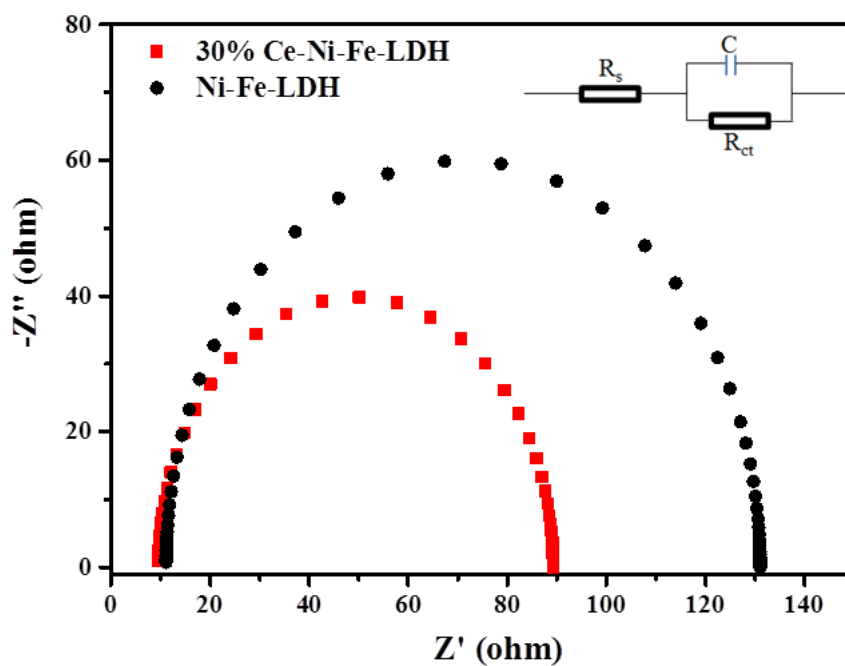


Fig. S18 Nyquist plots obtained by EIS at 1.55 V (vs. RHE) of Ni-Fe-LDH and 30%Ce-Ni-Fe-LDH (inset: equivalent RC circuit model).

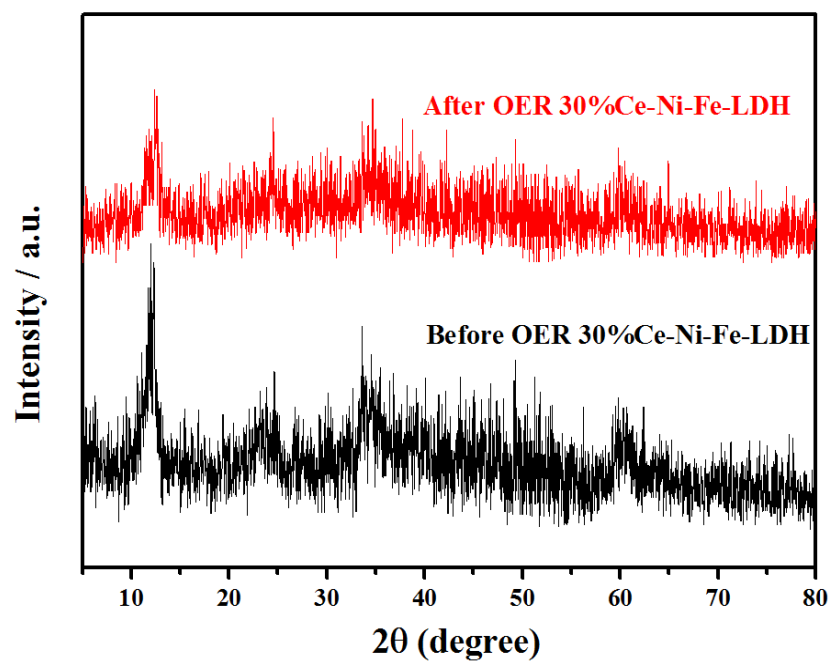


Fig. S19 XRD spectra of 30%Ce-Ni-Fe-LDH before and after the OER reaction.

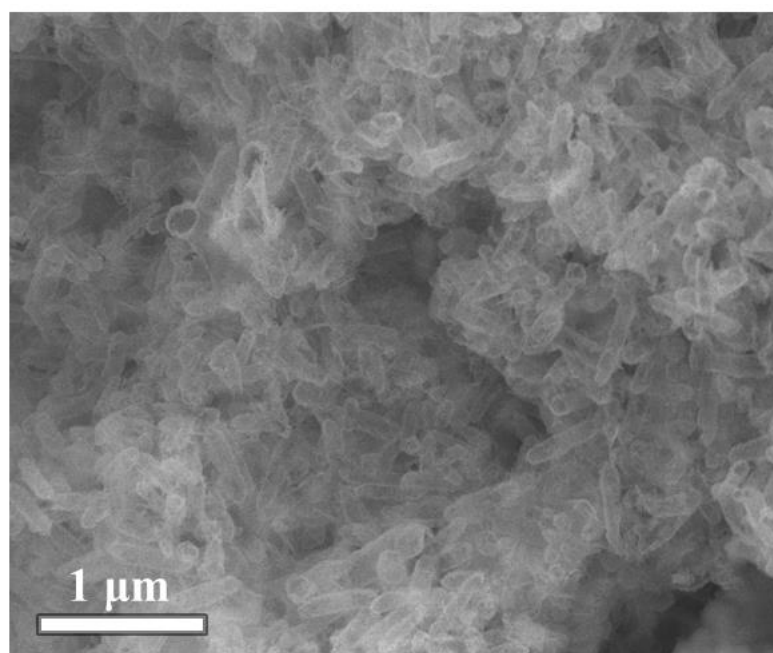


Fig. S20 The SEM of 30%Ce-Ni-Fe-LDH after 24 h test.

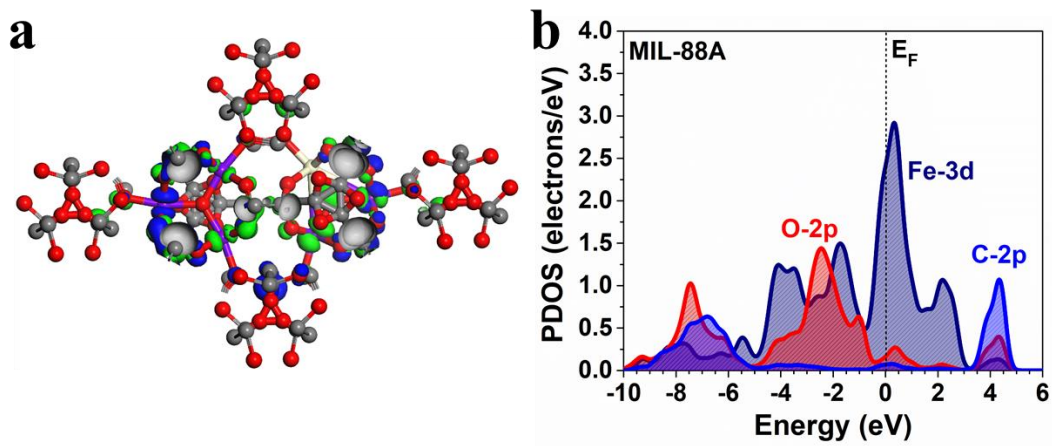


Fig. S21 a, The top view and side view of pristine MIL-88A. b, The PDOS of pristine MIL-88A.

6. Supplementary Tables

Table S1. The relative atom contents of elements in Ni-Fe-Ce-LDH/CNT from ICP-AES data.

Element	10%Ce-Ni-Fe-LDH	20%Ce-Ni-Fe-LDH	30%Ce-Ni-Fe-LDH	50%Ce-Ni-Fe-LDH
ratio of Ni: Fe: Ce	1.0:0.87:0.08	1.0:0.75:0.16	1.0:0.68:0.24	1.0:0.51:0.35

Table S2. Comparison of catalytic performance with reported MOF-Derived catalysts.

Catalyst	Support	Electrolyte	$\eta@10\text{ mA}$ cm^{-2} (mV)	Tafel slope (mV dec^{-1})	Ref.
CC@NiCo ₂ O ₄	carbon cloth	1M KOH	340	72	Adv. Energy Mater. 2017, 1602391.
NiCoP/C	GC	1M KOH	330	96	Angew. Chem. Int. Ed. 2017, 56,3897.
Co-IrCu ONC/C	GC	1M KOH	293	50	Adv. Funct. Mater. 2017, 27, 1604688.
Co ₃ O ₄ /Co-Fe oxide DSNBs	GC	1M KOH	297	61	Adv. Mater. 2018, 30, 1801211.
Ni-FeLDH hollow prisms	Ni foam	1M KOH	280	49.4	Angew. Chem. Int. Ed. 2018, 57, 172.
AN-CuNiFe	GC	1M KOH	224	44	Angew. Chem. Int. Ed. 2019, 58,4189.
Ni-Fe MOF nanosheet	Ni foam	1M KOH	240	34	Nat. Commun. 2017, 8, 15341.
MAF-X27-OH	GC	1M KOH	387	60	J. Am. Chem. Soc. 2016, 138, 8336.
Ligand mixed MOF-Fe	CC	1M KOH	288	39	Adv. Energy Mater. 2018, 8, 1801564.
FeTPyP-Co	GC	1M KOH	351		J. Am. Chem. Soc. 2016, 138, 3623.
MOF derived carbon nanocage	GC	1M KOH	330	51	Adv. Mater. 2017, 29, 1700874.
NNU-23	GC	1M KOH	365	77.2	Angew. Chem. Int. Ed. 2018, 57, 9660.
Co-MOF	GC	1M KOH	320	142	J. Am. Chem. Soc. 2014, 136, 13925.
Mn-Co	GC	1M KOH	320	52	Angew. Chem. Int. Ed. 2017, 56, 2386.
ZIF-67 derived hollow framework	GC	1M KOH	380	93	Nat. Energy 2016, 1, 1.
N-doped Co ₉ S ₈ /graphene	GC	1M KOH	280	82.7	Energ. Environ. Sci. 2016, 9, 1320-1326.
Co@N-CS/N-HCP@CC	carbon cloth	1M KOH	340	72	Adv. Energy Mater. 2019, 9, 1803918.
Fe-Ni@NC-CNTs	GC	1M KOH	274	56.4	Angew. Chem. Int. Ed. 2018, 57, 8921.
Co-NC/CF	GC	1M KOH	246	63	Energ Environ Sci , 2020. 13, 545
Fe ₃ -Co ₂ @GC	GC	1M KOH	300	43	J. Am. Chem. Soc. 2017, 139, 1778.
Co ₃ O ₄ C-NA	GC	1M KOH	240	70	J. Am. Chem. Soc. 2014, 136, 13925.
C-MOF-C2-900	GC	0.1M KOH	340	79	Adv. Mater. 2018, 30, 1705431.
Ni@NC-800	GC	1M KOH	280	45	Adv. Mater. 2017, 29, 1605957.
(Ni ₂ Co ₁) _{0.925} Fe _{0.075} -MOF-NF	GC	1M KOH	257	41.3	Adv. Mater. 2019, 31, 1901139
HXP@NC800	GC	1M KOH	307	48	J. Am. Chem. Soc. 2020, 142, 16, 7317.
aMOF-NC	GC	1M KOH	249	39.5	Angew. Chem. Int. Ed. 2020, 59, 3630.
30%Ce-Ni-Fe-LDH	GC	1M KOH	242	34	This work

Table S3. Comparison of catalytic performance with reported LDH catalysts.

Catalyst	Electrolyte	$\eta@10$ mA cm ⁻² (mV)	Tafel slope (mV dec ⁻¹)	Ref.
Ni-P porous Nanoplates	1 M KOH	300	64	Energy & Environ. Sci. 2016, 9 , 1246
CoSn(OH) ₆ Nanocube	1 M KOH	274	/	Energy & Environ. Sci. 2016, 9 , 473
CoV-LDH	1M KOH	250	44	Energy & Environ. Sci. 2018, 11 , 1736
NiFe Hydroxysulfide	0.1M KOH	286	81	Energy & Environ. Sci. 2020, 13 , 1711
NiV LDH	1 M KOH	318	50	Nat. Commun. 2016, 7 , 11981
e-FeCo LDH @GDY/NF	1 M KOH	216	43.6	Nat. Commun. 2018, 9 , 5309
Porous monolayer NiFe LDH	1 M KOH	230	47	Adv. Energy Mater. 2019, 9 , 1900881
NiFeCr LDH	1 M KOH	283	129	Adv. Energy Mater. 2018, 8 , 1703189
Thin NiFe LDH	1 M KOH	240	39	Adv. Energy Mater. 2017, 7 , 1602547
Au/NiFe LDH	1 M KOH	237	36	J. Am. Chem. Soc. 2018, 140 , 3876
Ag@Co(OH) _x / CC	1 M KOH	250	76	Angew. Chem. Int. Ed. 2020, 132 , 7312
30%Ce-Ni-Fe- LDH	1M KOH	242	34	This work

Table S4. The TOF of the as-prepared catalysts.

Sample	TOF ($\times 10^{-2}/s^{-1}$)
NiFe-LDH	0.32
5%Ce-Ni-Fe-LDH	0.41
10%Ce-Ni-Fe-LDH	0.50
20%Ce-Ni-Fe-LDH	0.62
30%Ce-Ni-Fe-LDH	1.12
40%Ce-Ni-Fe-LDH	0.96
50%Ce-Ni-Fe-LDH	0.18

7. References

- [S1] S. J. Clark, M. D. Segall, C. J. Pickard, P. J. Hasnip, M. J. Probert, K. Refson and M. C. Payne, *Z Kristallogr.*, 2005, **220**, 567.
- [S2] D. Vanderbilt, *Phys. Rev. B.*, 1990, **41**, 7892.
- [S3] J. P. Perdew, K. Burke and M. Ernzerhof, *Phys. Rev. Lett.*, 1996, **77**, 3865.
- [S4] P. J. Hasnip and C. J. Pickard, *Comput. Phys. Commun.*, 2006, **174**, 24.
- [S5] J. P. Perdew, J. A. Chevary, S. H. Vosko, K. A. Jackson, M. R. Pederson, D. J. Singh and C. Fiolhais, *Phys. Rev. B.*, 1992, **46**, 6671.
- [S6] J. D. Head and M. C. Zerner, *Chem. Phys. Lett.*, 1985, **122**, 264.
- [S7] M. I. J. Probert and M. C. Payne, *Phys. Rev. B.*, 2003, **67**, 075204.